

# Permeability Evolution of Propped Artificial Fractures in Green River Shale

Xiang Li<sup>1</sup>  · Zijun Feng<sup>1,2</sup> · Gang Han<sup>3</sup> · Derek Elsworth<sup>1,4</sup> · Chris Marone<sup>4</sup> · Demian Saffer<sup>4</sup> · Dae-Sung Cheon<sup>5</sup>

Received: 8 December 2015 / Accepted: 11 February 2017 / Published online: 23 February 2017  
© Springer-Verlag Wien 2017

**Abstract** This paper compares the evolution of permeability with effective stress in propped fractures in shale for native CH<sub>4</sub> compared with that for sorbing CO<sub>2</sub>, slightly sorbing N<sub>2</sub> and non-sorbing He. We examine the response for laboratory experiments on artificial propped fractures in Green River Shale to explore mechanisms of proppant embedment and fracture diagenesis. Split cylindrical specimens sandwich a proppant bead-pack at a constant confining stress of 20 MPa and with varied pore pressure. Permeability and sorption characteristics are measured with the pulse transient method. To explore the effect of swelling and embedment on fracture surface geometry, we measure the evolution of conductivity characteristics for different proppant geometries (single layer vs. multilayer), gas saturation and specimen variation in order to simulate both production and enhanced gas recovery. The resulting morphology of embedment is measured by white light interferometry and characterized via surface roughness parameter of mean, maximum and root-mean-square

amplitudes. For both strongly (CO<sub>2</sub>, CH<sub>4</sub>) and slightly adsorptive gases (N<sub>2</sub>), the permeability first decreases with an increase in gas pressure due to swelling before effective stress effects dominate above the Langmuir pressure threshold. CO<sub>2</sub> with its highest adsorption affinity produces the lowest permeability among these three gas permeants. Monolayer propped specimens show maximum swelling and lowered  $k/k_0$  ratio and increased embedment recorded in the surface roughness relative to the multilayered specimens. Permeabilities measured for both injection and depletion cycles generally overlap and are repeatable with little hysteresis. This suggests the dominant role of reversible swelling over irreversible embedment. Gas permeant composition and related swelling have an important effect on the permeability evolution of shales.

**Keywords** Permeability · Fracture · Shales · CO<sub>2</sub> · Adsorption · Swelling · Roughness

## 1 Introduction

Gas transport in shale is different from that in other rock types due to gas sorption-induced shale swelling (Wang et al. 2011; Kumar et al. 2016). Mature shale gas plays respond similarly to coalbeds (Pellenq et al. 2012) with regard to swelling and permeability response. Adsorption of sorbing gases (e.g., CO<sub>2</sub>) in micropores results in matrix swelling, permeability reduction in natural fractures and the restriction of fluid flow even when the porous medium is mechanically unconstrained. However, this potential loss of permeability is temporary. Once it reaches a threshold pressure, equivalent to approximately double the Langmuir pressure, permeability will rebound and typically increase

✉ Xiang Li  
xz1111@psu.edu

<sup>1</sup> John and Willie Leone Family Department of Energy and Mineral Engineering, EMS Energy Institute and G3 Center, The Pennsylvania State University, University Park, PA 16802, USA

<sup>2</sup> Department of Mining Engineering, Taiyuan University of Technology, Taiyuan 030024, Shanxi, China

<sup>3</sup> Aramco Services Company, Houston, TX 77096, USA

<sup>4</sup> Department of Geosciences, EMS Energy Institute and G3 Center, The Pennsylvania State University, University Park, PA 16802, USA

<sup>5</sup> Geologic Environment Division, Underground Space Department, KIGAM, Daejeon 305-350, Korea

as the effective stress decreases (Siriwardane et al. 2009; Somerton et al. 1975).

Shales, as unconventional reservoirs with extremely low permeability, are often hydraulically fractured with proppant-slurry injected into the hydraulic fractures to create and maintain enhanced permeability. Both experiments (Piggott and Elsworth 1993; Walsh 1981) and numerical models (Bai and Elsworth 1994; Elsworth and Yasuhara 2010; Yasuhara and Elsworth 2008; Yasuhara et al. 2006) may be used to illuminate the evolution of permeability under different mechanical, chemical, thermal and hydraulic conditions. Effective stresses in shales may reduce fracture aperture due to the embedment of proppants into the surface of the hydraulic fracture (Freeman et al. 2009; Lacy et al. 1997). Morphological analyses of surface asperities have been used to determine the effect of stress on proppant breakage and embedment (Cooke 1977) and to determine the role of fracture roughness. Results show that surface asperities have little impact on the evolution of fracture permeability when there is a high concentration of proppant filling the fracture (Stoddard et al. 2011). Alramahi and Sundberg (2012) proposed an analytical model to predict the stress-dependent conductivity of hydraulic fractures based on laboratory measurements of proppant embedment. They also studied the relations between rock mineralogy, mechanical properties, fluid composition and proppant embedment. The results show a close correlation between the proppant embedment at a given stress and the rock stiffness which, in turn, is affected by the mineral content. These relations can be used to predict the severity of conductivity loss due to proppant embedment as a function of rock properties.

Although the behavior of artificial fractures in granite, limestone and carbonates has been reported in the literature, the response of proppant packs in artificial fractures in shales is less well defined. This is due to the complex behavior of shale reservoirs and their relatively recent utilization. This paper compares the permeability evolution of native CH<sub>4</sub> with that of sorbing CO<sub>2</sub>, slightly sorbing N<sub>2</sub> and non-sorbing He, as a function of pore pressure and using propped artificial fractures in Green River Shale. To explore the effect of swelling and embedment on surface geometry, we measure the evolution of conductivity characteristics with different proppant geometries (single layer vs. multilayered specimens), gas saturation and specimen heterogeneity. These experiments are analogs for proppant embedment and fracture diagenesis in shales during production and enhanced gas recovery.

## 2 Experimental Methods

We saturate longitudinally split cores of shale separated by a monolayer (high adsorption influence) or four layers (low adsorption influence) of proppant with He, N<sub>2</sub>, CH<sub>4</sub> and

CO<sub>2</sub>. We measure permeability evolution via pulse tests in which mean gas pressure is first incremented (injection process) then decremented (depletion process). We then examine the morphology of the fracture surface due to embedment of the proppant. Finally, we use these observations to define the mechanistic response of fractures in swelling shales containing proppant packs.

### 2.1 Apparatus

The observations reported in this study are measured with a standard triaxial apparatus arranged for flow-through/pulse permeability testing and hydraulic fracturing (Fig. 1a). A triaxial core holder (Temco) accommodates the membrane-sheathed cylindrical specimens (1 inch in diameter and 2 inches in length) and applies independent loading in the radial and axial directions.

Constant confining (20 MPa) and axial stresses (10 MPa) are applied separately with two syringe pumps (Isco 500D) with control to  $\pm 0.07$  MPa. Upstream and downstream gas reservoirs are used for pulse testing of permeability. Gas pressure is applied through the upstream reservoir (Fig. 1b) with the downstream reservoir  $\sim 1$  MPa lower than the upstream pressure. This enables the measurement of H<sub>2</sub>, N<sub>2</sub>, CH<sub>4</sub> and CO<sub>2</sub> permeabilities through both monolayer and multilayer (four layers) proppant packs in the artificial fracture.

The cylindrical specimen is held within the core holder between upstream and downstream stainless steel platens. Each platen connects a flow line to fluid distributors. The specimen and axial platens are isolated from the confining fluid by a Viton rubber jacket. The end plugs are connected to two small-volume stainless steel gas reservoirs through tubing and isolating valves. Upstream and downstream fluid pressures are measured by pressure transducers (Omega PX302-2KGV and Omega PX302-5KGV) to a resolution of  $\pm 0.03$  MPa. The gas-pressurized upstream reservoir is discharged through the specimen to the downstream reservoir with equilibration time defining the permeability of the specimen (Brace et al. 1968; Hsieh et al. 1981). Volume change effects due to the high compressibility of gas in the reservoirs are minimized by immersing the gas reservoirs in water baths to maintain constant ambient temperature (Fig. 1b). Pressure, flow rate and fluid volume signals obtained from the syringe pumps are controlled and/or recorded through a National Instruments Labview data acquisition system and a serial connection (RS-232) between the pumps and the logging computer. The signals are then logged digitally at sampling rates from 1 Hz to 1 kHz using Labview.

### 2.2 Specimen Preparation

A cylindrical specimen—1 inch in diameter and two in length—is axially split by a diamond trimming saw into two

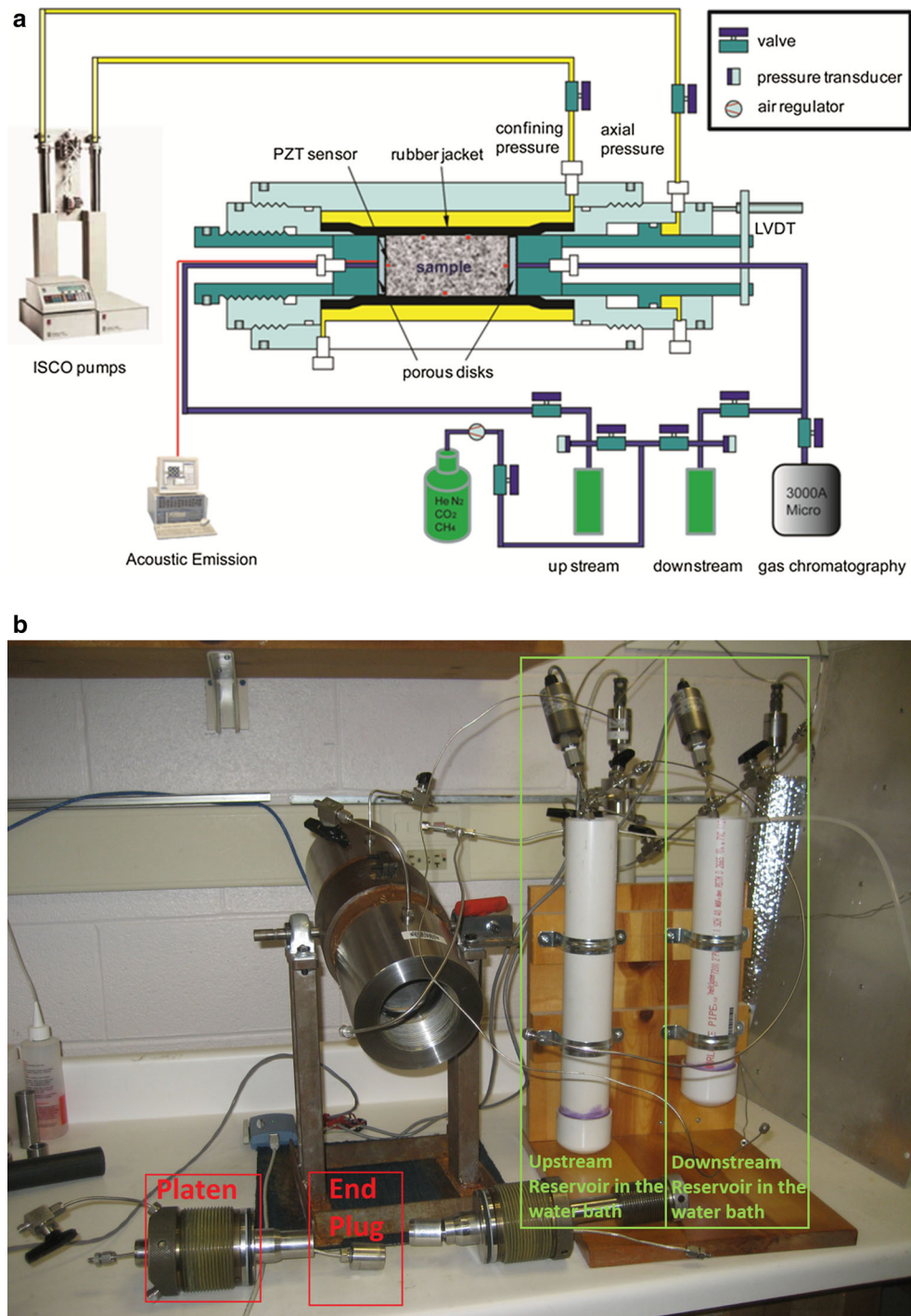


**Fig. 1** a Schematic of pulse test transient/hydraulic fracturing system (Wang et al. 2011). Sample sealed by a rubber jacket is placed in the cell with platens fixed at the ends. Syringe pumps supply confining and axial pressure. Fluid flow from an upstream to a downstream

reservoir enables pulse permeability to be measured. b Pulse test transient system. Containment vessel with platen and fluid feed assembly and cell end-caps in foreground

symmetric half-cylinders. The surfaces are polished with grinding medium and then sandwiched with either a single layer or four layers of carbolite 40/80 mesh proppant. The pure

gases used in this study are CO<sub>2</sub> and CH<sub>4</sub> at purities of 99.995%, He at a purity of 99.999% and N<sub>2</sub> at a purity of 99.9999%.

### 2.3 Standard Test Procedure

The pressure transient or pulse method is used to conduct the permeability measurements. In a typical experiment, the specimen is placed into the triaxial core holder and both confining stress and axial stresses are applied and then held constant. The core assembly is then vacuum desaturated to evacuate any remnant traces of the previously tested. A pressure increment is then applied to the upstream reservoir and discharged through the specimen to the downstream gas reservoir. The time taken for the upstream reservoir to discharge into the downstream reservoir and to establish a new equilibrium pressure is measured. This pattern is repeated for multiple cycles using the gas permeants to establish a relation between permeability and gas pressure. In this study, applied gas pressures range between 2 and 12 MPa.

The pressure decay rate in the upstream reservoir and the pressure increase rate in the downstream reservoir are used to calculate permeability. The pulse decay behavior depends on the permeability, the dimensions of the specimen and reservoirs and also the physical properties of the permeants. The pressure transient method is used to determine permeability (Brace et al. 1968; Hsieh et al. 1981). The evolution of the pressure pulse can be expressed as follows:

$$P_{\text{up}}(t) - P_{\text{dn}}(t) = (P_{\text{up}}(t_0) - P_{\text{dn}}(t_0))e^{-\alpha t} \quad (1)$$

$$k = \frac{\alpha \mu L V_{\text{up}} V_{\text{dn}}}{A(V_{\text{up}} + V_{\text{dn}})K} \quad (2)$$

$$K = v^2 \rho \quad (3)$$

where  $P_{\text{up}}(t) - P_{\text{dn}}(t)$  is the pressure difference between the upstream and downstream reservoirs at time  $t$ ; and  $P_{\text{up}}(t_0) - P_{\text{dn}}(t_0)$  is the initial pressure difference between the upstream and downstream reservoirs at time  $t_0$ ;  $\alpha$  is the slope of the pressure decay  $P_{\text{up}}(t) - P_{\text{dn}}(t)$  (semi-log) against time;  $A$  and  $L$  in Eq. (2) are the cross-sectional area and length of the specimen, respectively, which define the dimensions of the specimen;  $\mu$ ,  $V_{\text{up}}$  and  $V_{\text{dn}}$  are the dynamic viscosity of the gas, and the volume of the upstream reservoir and the downstream reservoir, respectively.  $K$ ,  $v$  and  $\rho$  are the bulk modulus, sonic velocity and fluid density of the gas permeant at defined pressure and ambient temperature. Permeability  $k$  then is calculated from Eq. (2) where it is the only unknown.

## 3 Results

A variety of factors are examined in this study to explore permeability evolution with different gas permeants. These factors include the effect of sorption-induced swelling, the

duration of gas exposure and saturation, the injection/depletion process and natural variation between different specimens.

### 3.1 Prior Results on Sorbing Media

The fluid transport properties of shale vary with gas composition. Both changes in effective stress and the swelling of an organic phase control shale permeability (Heller and Zoback 2014). Shale can be considered as a dual porosity system with matrix and fracture. Adsorptive gases ( $\text{CO}_2$ ,  $\text{CH}_4$  and  $\text{N}_2$ ) are sorbed in the shale matrix causing it to swell, reducing permeability as open fractures are compressed. Porosity and volumetric strain are functions of gas pressure with the strain being larger for  $\text{CO}_2$  and  $\text{CH}_4$  (adsorptive gas) than He (non-adsorptive gas) demonstrating gas adsorption-induced swelling for the shales (Chen et al. 2015).

This study examines the evolution of permeability of propped fractures in the presence of permeants—He,  $\text{N}_2$ ,  $\text{CH}_4$  and  $\text{CO}_2$ —as natural in situ or stimulating fluids. Among these four gas permeants,  $\text{CO}_2$  has the highest adsorptive affinity, followed by  $\text{CH}_4$  and then  $\text{N}_2$ . He is essentially a non-sorbing gas.  $\text{CO}_2$  has the highest adsorption-induced swelling and therefore the largest potential impact on permeability at any defined low pressure. The influence of gas adsorption on permeability under constant external stress results in a typical U-shaped curve as pore pressure increases (Fig. 2). In Fig. 2, permeability first decreases due to adsorption-induced matrix swelling via the narrowing of fracture aperture before the magnitude of this effect is overtaken by the dilative effects of reduced effective stresses. This latter switch in response results in a permeability increase, a phenomenon known as

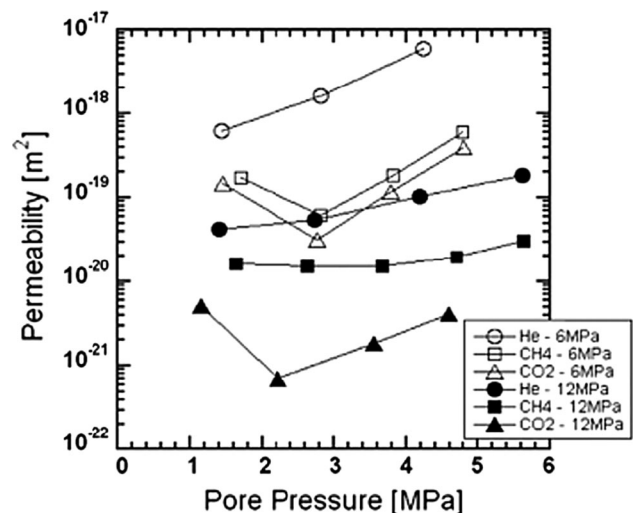


Fig. 2 Typical adsorptive gas permeability behavior (Wang et al. 2011)

‘permeability rebound,’ and attributed to a reopening of the fracture due to an increase over time of the fluid pressure in the fracture. In contrast, for non-sorbing gas like He, permeability increases as pore pressures increases due solely to the reduction in effective stress.

### 3.2 Experimental Results

Experiments are conducted on Green River Shale under constant total (external) confining stress of 20 MPa by first incrementing, and then decrementing, the gas pressure in ~1 MPa steps. The experiments are conducted by injecting (increasing gas pressure) He and then retreating to the original pressure. This is followed by a similar cycle with N<sub>2</sub>, CH<sub>4</sub> and then CO<sub>2</sub> to compare the permeability evolution due to different gases on the same specimen and also the difference between injection and depletion processes for each permeating fluid. For each gas composition, except for He, at least two different specimens are tested to investigate the natural variation between different specimens. The effect of swelling on permeability is studied by comparing the CO<sub>2</sub> permeability evolution in propped monolayer and multilayered specimens. The specimens are sandwiched with either a single layer or four layers of carbolite 40/80 mesh proppant (Fig. 3). The effect of gas exposure and saturation is investigated by exposing the specimen to CO<sub>2</sub> for different durations.

#### 3.2.1 Effect of Different Gas Permeants

The permeabilities of a monolayer-propped fracture to both non-sorbing gas (He) and sorbing gas (N<sub>2</sub>, CH<sub>4</sub> and CO<sub>2</sub>)

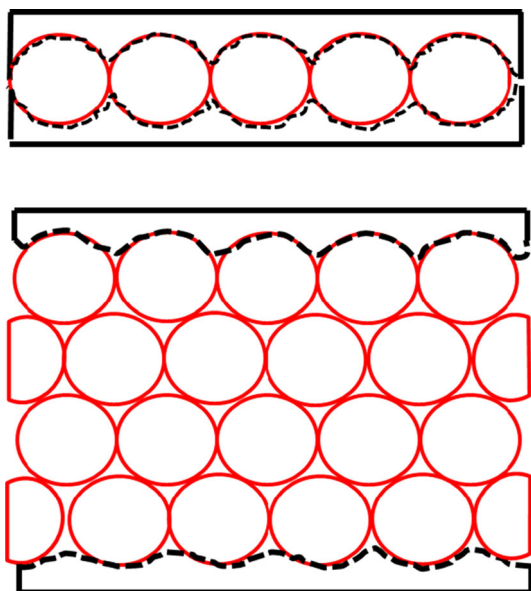


Fig. 3 Illustration of monolayered versus multilayered specimen

and show different trends. For non-sorbing gas, permeability increases with pore pressure due to the decrease of effective stress, but for sorbing gas, permeabilities first decrease and then recover as pore pressure increases above a threshold of approximately double the Langmuir pressure (Kumar et al. 2016; Fig. 4). The extent of the decrease and rebound depends on the adsorptive affinity of the gases. Gas with a higher adsorptive affinity results in a larger volume change and a greater possible change in permeability. Under constant confining pressure, an increase in gas pressure (reduction of effective stress) dilates the fracture and therefore increases the permeability. However, adsorption-induced swelling results in an enlarged matrix, closing the fracture and reducing permeability. The net change in permeability depends on the competing effects of these two processes. Figure 4 indicates that as pore pressure increases, the reduction in permeability induced by swelling first dominates. However, for Langmuir-type swelling, the swelling rate gradually decreases as pore pressure reaches double the Langmuir pressure. Subsequently, permeability increases with the reduction in effective stress, which ultimately dominates over the influence of swelling.

Figure 5 shows that the He permeability (non-sorbing gas) for our monolayer proppant configuration increases by 1.2 times as the gas pressure increases from 2.2 to 12.2 MPa. The sorbing gases N<sub>2</sub>, CH<sub>4</sub> and CO<sub>2</sub> all show the typical U-shaped curve with N<sub>2</sub> having the highest permeability, followed by CH<sub>4</sub> and then CO<sub>2</sub>. The net

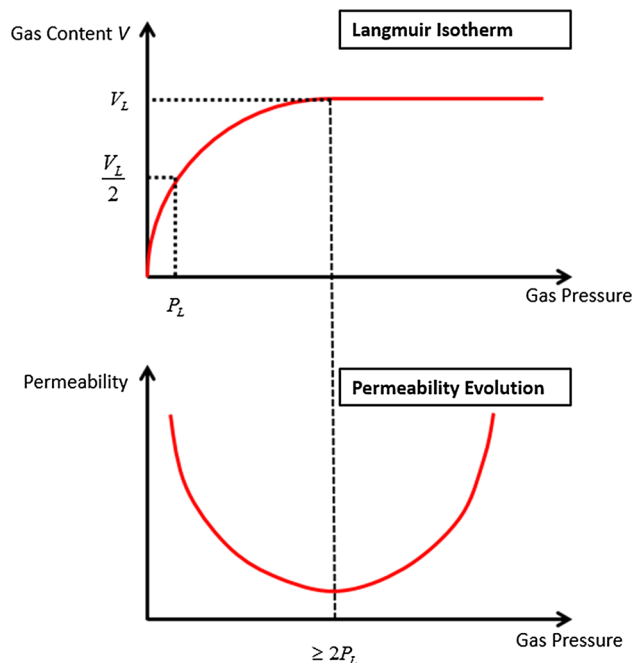
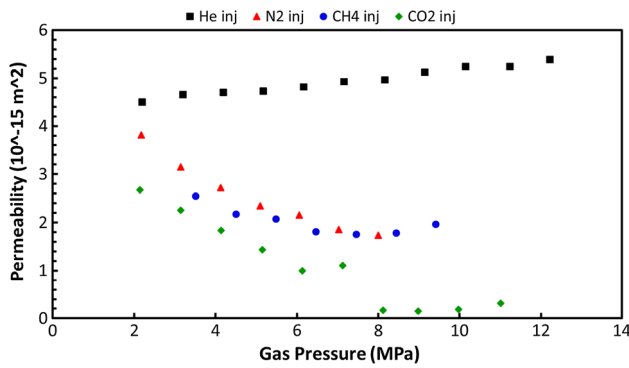


Fig. 4 Relation between the Langmuir pressure threshold and the trough of the U-shaped curve for an adsorptive gas



**Fig. 5** Permeability evolution in GRS specimens upon injection of He, N<sub>2</sub>, CH<sub>4</sub>, CO<sub>2</sub>. The observations are made by incrementing gas pressure at constant confining pressure of 20 MPa and with mono-layer proppant

permeability change is controlled by the competition of permeability reduction induced by swelling with permeability enhancement caused by the reduced effective stress. For N<sub>2</sub>, the permeability decreases by 54% for gas pressures in the range 2.2–8 MPa. A permeability rebound for N<sub>2</sub> is not observed in this specimen due to the upper limit of the gas pressure in this single test. This is observed in Fig. 11a simply because the gas pressure is sufficiently high. For CH<sub>4</sub>, permeability decreases by 31% when the gas pressure increases from 3.5 to 7.5 MPa and then rebounds to 77% of the initial permeability at a final gas pressure of 9.4 MPa. For CO<sub>2</sub>, permeability first decreases by 63% for pore pressures from 2.1 to 6.1 MPa and then increases above 6.1 MPa. The downward shift of the high-pressure portion of the U-shaped curve for CO<sub>2</sub> is due to a decrease in the compressibility as the fluid transitions from a gas to a liquid above ~8 MPa (experimental temperature is room temperature; ~21 °C). The threshold (minimum) in the U-shaped curve for CO<sub>2</sub> is lower than that for CH<sub>4</sub> (Fig. 5), indicating that the Langmuir pressure of CO<sub>2</sub> is lower than that of CH<sub>4</sub>, consistent with previous studies (Heller and Zoback 2014).

### 3.2.2 Effect of Adsorption-Induced Swelling

To investigate the relative effects of adsorption-induced swelling in the shale, we contrast the performance of a multilayered propped specimen (four layers) with a monolayer propped specimen. Figure 6 shows the permeability evolution in these two cases for the injection of CO<sub>2</sub>. The permeability for the monolayer propped fracture is slightly lower than that of the multilayer propped fracture.

A bead-packed channel with multiple-layers of proppant (Fig. 7a) can be considered as a plane channel (Fig. 7b) of aperture  $b$ , filled with a porous material with permeability

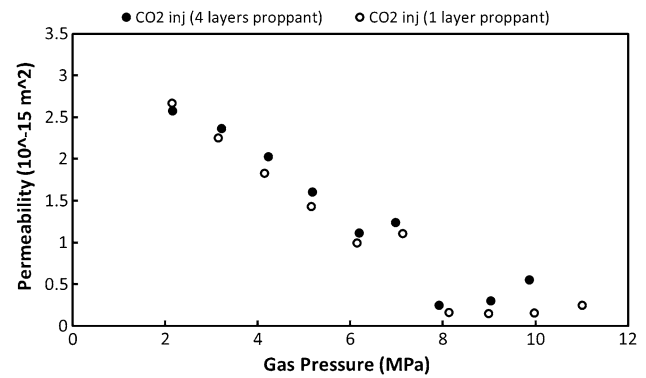


**Fig. 6** Permeability evolution of multilayered and monolayered propped fractures under the injection of CO<sub>2</sub>

$k_f$  with fluid flow around a packed assemblage of spheres of uniform size as

$$Q = \frac{\Delta P}{\mu L} b k_f W \quad (4)$$

where  $\mu$  is the temperature-dependent dynamic viscosity of the fluid [ $M L^{-1} T^{-1}$ ],  $L$  is the length of the fracture [L],  $W$  is the width of the fracture [L],  $Q$  is the flow rate [ $L^3 T^{-1}$ ],  $dP$  is the differential pressure [ $M T^{-2} L^{-1}$ ], and  $b$  is the hydraulic aperture of the fracture [L]. As an extension of the Poiseuille equation, which gives the pressure drop for an incompressible and Newtonian fluid in laminar flow passing through a long cylindrical pipe of constant cross section, the parallel plate approximation allows one to directly convert the flow rate of a fluid between two planes to an equivalent hydraulic aperture.

Slichter (1899) performed a theoretical analysis of fluid flow through a packed bed of spheres of uniform size and introduced packing as a factor influencing permeability, as,

$$k_f = \frac{10.2d^2}{k_s} \quad (5)$$

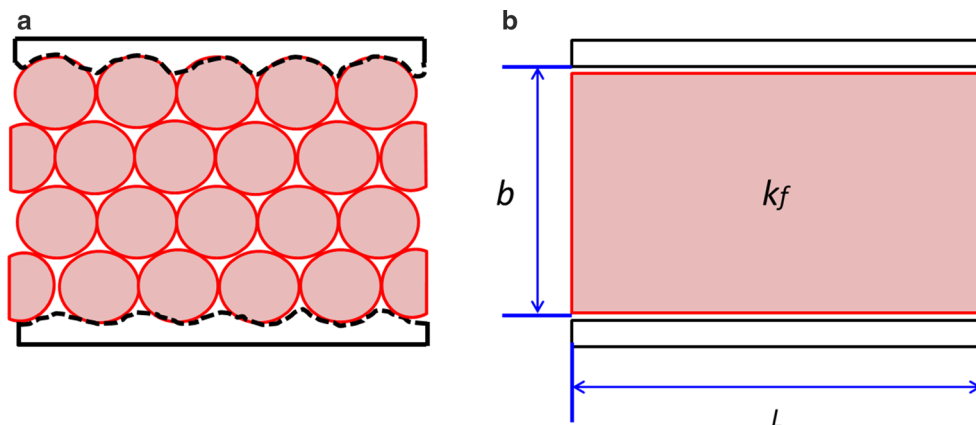
where  $d$  is the sphere diameter [L] and  $k_s$  is a packing constant that is a function of porosity,  $\phi$  (for hexagonal packing,  $\phi = 26\%$  and  $k_s = 84.4$ ; for cubic packing,  $\phi = 45\%$  and  $k_s = 13.7$ ). One well-known correlation (Kozeny 1927; Carman 1937) considers bundled capillaries to determine permeability as:

$$k_f = \frac{\phi \delta^2}{8\tau} \quad (6)$$

where  $\phi$  is the porosity,  $\delta$  is the mean capillary diameter,  $\tau$  is the tortuosity defined as the square of the ratio between the effective channel length  $L_e$  due to the tortuous path and the length  $L$  of the porous body ( $\tau \equiv (L_e/L)^2$  with  $\tau = 25/12$  for a bed of uniform particles).

This can also be expressed as

**Fig. 7** Configuration of parallel plate channel



$$k_f = \frac{\phi^3 d^2}{72\tau(1 - \phi)^2} \tag{7}$$

This equation results from the combination of Darcy’s and Poiseuille’s laws (Haro 2013). While Darcy’s law macroscopically quantifies fluid flow, Poiseuille’s law considers the parabolic flow velocity profile of a viscous fluid in a straight-circular tube. Specifically, within the Kozeny–Carman formalism, let us assume that  $\tau$  varies with porosity  $\phi$ . Consider one candidate equation for this dependence:

$$\tau = (1 + \phi^{-1})/2 \tag{8}$$

as defined theoretically by Berryman (Berryman 1981).

For a channel filled with a bed of uniform particles representing the monolayered specimen, the porosity can be readily calculated as 47.64%. For a face-centered cubic (FCC) geometry which represents the multilayered specimen, the porosity is in the range 25–50%; therefore, if we use Eq. (8) for  $\tau$ , then the ratio between the permeability of a monolayer propped fracture and that of the multilayered specimen is 0.57 (if the porosity of the multilayered specimen is 50%) or 30 (if the porosity of the multilayered specimen is 25%). As shown in Fig. 6, in this experiment, the ratio between the permeability of the monolayered specimen and that of the multilayered specimen is ~0.9, which falls within this range (0.57–30).

The modeling of porosity–permeability relations may be case in the formalism of Rose (1945):

$$k \sim \phi^m \tag{9}$$

where  $m$  is an exponent typically determined empirically. For the parallel plate approximation,  $m = 3$ ; and for the Kozeny–Carman formalism,  $m = 1$ ; other arguments consider that (Chandra 2012) for a fracture filled with grains,  $m$  can be as high as ~9.8–17.8. Therefore, an observed change in permeability can be a proxy for changes in porosity. If we assume that the relative particle to particle geometry changes little during the permeability evolution,

then the change in permeability/porosity is mainly due to swelling that removes the pore space in the proppant-filled fracture during the experiment when the fracture is exposed to adsorptive gases. Figure 8 shows that the multilayer propped specimen is less sensitive to swelling compared to the monolayer specimen, which exhibits a lower  $k/k_0$  ratio. The permeability evolution indicates that the permeability of the multilayer propped fracture decreases by 58%, whereas for the monolayer propped fracture, this value is 63%. This comparison is also supported by morphological analysis of embedment in the fracture surfaces, discussed later.

### 3.2.3 Effect of Gas Exposure and Gas Saturation

To investigate the effect of gas exposure and saturation, which is defined as the ratio of the volume of fluid to pore volume, we exposed the monolayered specimen to the gas permeants for different durations (up to ~20 h) at an equilibrium gas pressure of ~3.7 MPa. Two gases are used: non-sorbing He and strongly sorbing CO<sub>2</sub>. Although the permeability to sorbing gas in coal is found to be a function of gas exposure time (Shimada et al. 2005), as shown in Fig. 9, our data indicate that for the exposure

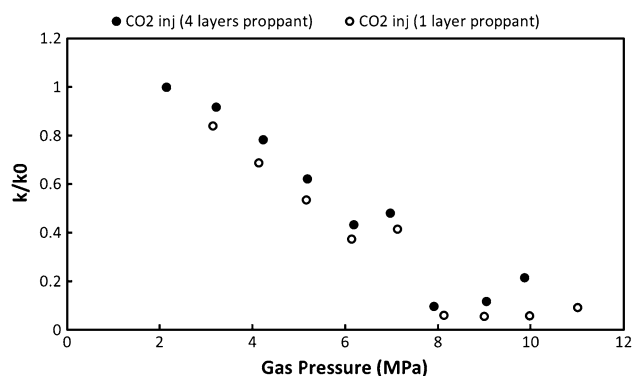


**Fig. 8**  $k/k_0$  ratio between multilayers (four layers) and monolayer propped fracture under the injection of CO<sub>2</sub>

durations explored (up to  $\sim 20$  h) there is no significant influence on permeability for Green River Shale. This is because the intrinsic permeability of the rock ( $10^{-19}$  m<sup>2</sup>) is too low for significant gas flow from the fracture into the specimen interior (distinct from the fracture surface) during the duration of the experiment. Therefore, the swelling due to CO<sub>2</sub> adsorption is restricted primarily to the matrix near the fracture. However, the impact on embedment is appropriately probed in these experiments. The non-saturated case (saturation time = 0 h) and fully saturated case (saturation time =  $\sim 20$  h) exhibit similar permeability for both the sorbing and non-sorbing gases. CO<sub>2</sub> has a lower permeability compared to He due to its adsorptive affinity to shale, which results in swelling of the rock matrix and hence decreased permeability. The results imply that 20 h is an insufficient duration to cause swelling of the specimen interior (distinct from the fracture surface) considering the low permeability of GRS and low diffusion coefficient to CO<sub>2</sub>. Exposure time might have an effect, but only over timescales  $>20$  h.

### 3.2.4 Consistency Between Injection and Depletion

Once well production declines to nearzero productivity, well stimulation including hydraulic fracturing may be used to increase production. Enhanced Gas Recovery (EGR) is another method to boost production by utilizing the high adsorptive affinity of gases like CO<sub>2</sub> to chemically displace CH<sub>4</sub>. To explore this process in our study, experiments are conducted on a monolayer propped specimen by injecting (increasing gas pressure) gas permeants and then retreating to the original pressure to simulate EGR and also the production–depletion processes.

Figure 10 shows similar trends in permeability evolution between injection and depletion processes for all of the gas permeants. Notably, during the CO<sub>2</sub> depletion process, permeability is unstably high at the liquid-to-gas transition pressure for CO<sub>2</sub> ( $\sim 7$  MPa). The same phenomenon is also observed in the depletion process for the multilayered

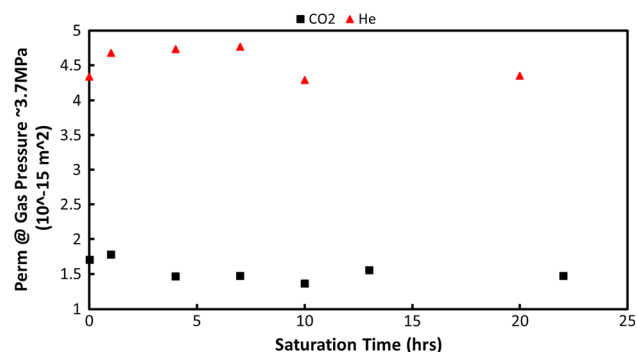


**Fig. 9** Effect of saturation time on permeability with He and CO<sub>2</sub> as gas permeants

specimen (figure not shown). This is due to the sudden volume increase causing a high apparent permeability when fluid transits from liquid to gas state due to a storage effect. During the depletion process, where CO<sub>2</sub> pressure decreases, it transits into a condensation region where fluid volume increases, but pressure remains constant (Fig. 11). This was first noted by Andrews (1869), who showed the effect of pressure on volume of CO<sub>2</sub> at different temperatures. Figure 11 shows the partial pressure of CO<sub>2</sub> versus volume for various constant temperatures. The state of the CO<sub>2</sub> depends on its pressure, volume and temperature. The liquid state can only exist at or below the critical temperature. Considering the 21 °C (ambient temperature in our experiment) isotherm at low applied pressure, the CO<sub>2</sub> is gaseous (vapor) and generally exhibits the characteristics of a gas (Boyle's Law) from point A to B. Beyond point B, a very slight increase in pressure results in a change from vapor to a liquid. This is the phenomenon of saturation. Specifically, from point B to C, the pressure is virtually constant while the volume is decreasing and at point C the substance is solely liquid. The spontaneous increase in pressure at point C is represented as a vertical curve where very little change in volume is possible as the liquid is virtually incompressible. When the above process reverses, such that the pressure decreases and reaches the condensation region (from point C to B) where saturated vapor and liquid coexist, the sudden increase in volume results in a sudden decrease in fluid density, which in turn results in a decrease in bulk modulus and an increase in apparent permeability (Eqs. 2, 3) as the traditional permeability relation (Eqs. 2, 3) does not account for the phase transition.

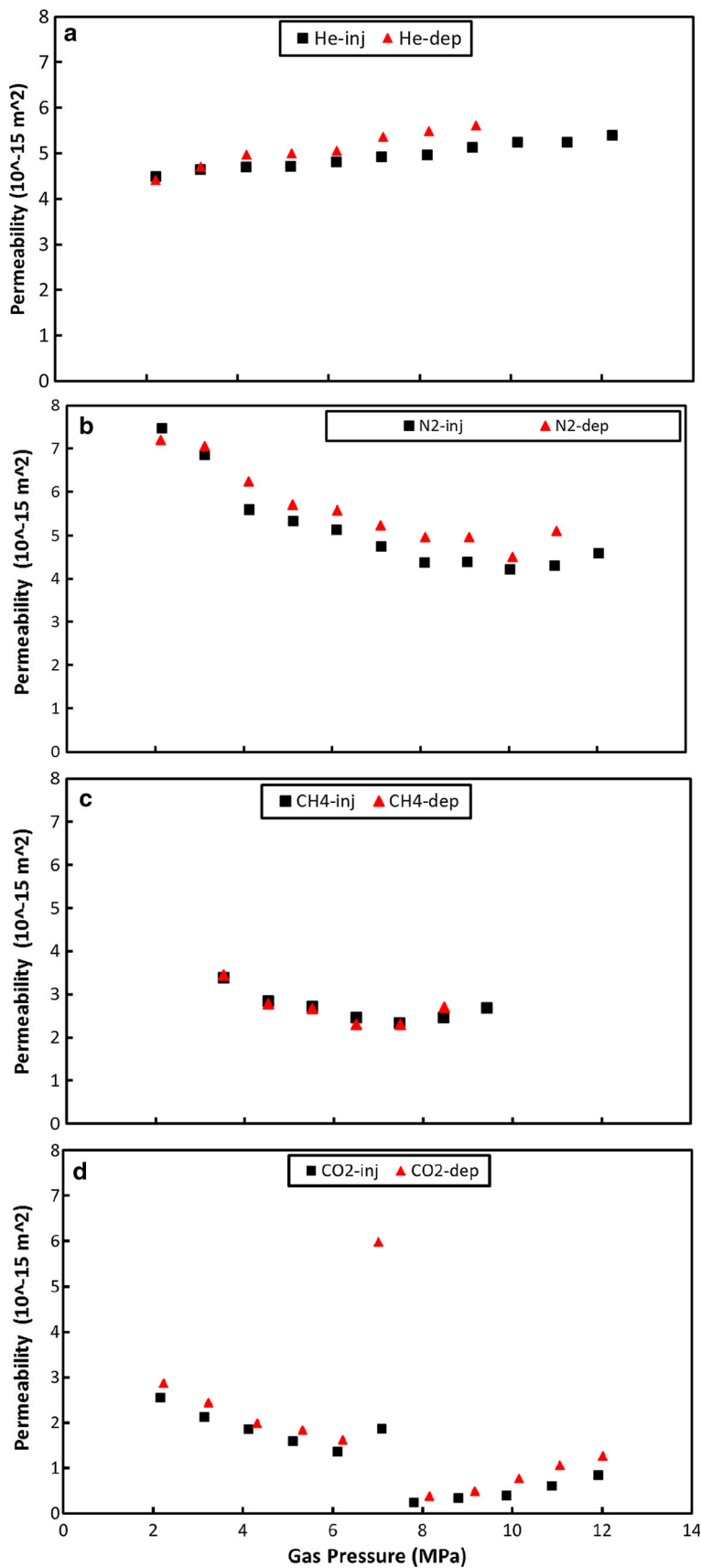
### 3.2.5 Natural Variation Between Different Specimens

We tested two different monolayer propped specimens for N<sub>2</sub>, CH<sub>4</sub> and three for CO<sub>2</sub> to investigate the effect of natural variation between specimens (Fig. 12). Results show that the differences in permeability between otherwise identical specimens and experiments run with N<sub>2</sub>, CH<sub>4</sub> and CO<sub>2</sub> are of the order of  $\sim 1.3$ –2 times. Previous work suggests that differences in permeability between specimens can be up to two orders of magnitude and may be attributed to the mineral composition (organic matter, clay, heavy minerals) and lithology (Kumar et al. 2016).

### 3.2.6 Proppant Embedment Morphological Analysis

Proppant embedment morphologies are measured using a Zygo NewView 7300 scanning white light interferometer with a scan speed of up to 135  $\mu\text{m/s}$  and sub-nanometer resolution. Figure 13 shows the effects of proppant embedment on the specimen after the test.

**Fig. 10** Permeability evolution during injection and depletion processes with different gas permeants



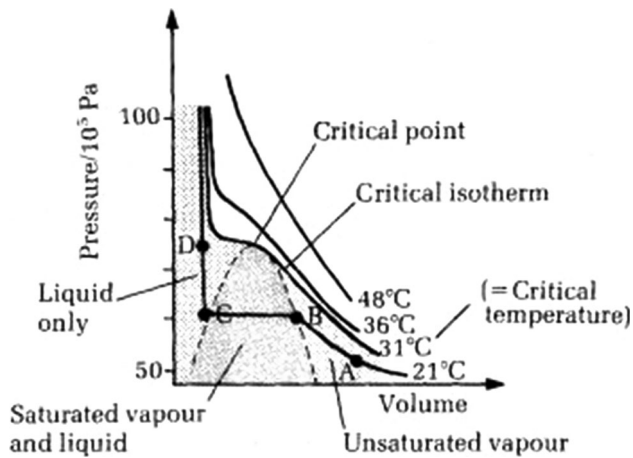


Fig. 11  $p, V$  isothermal for  $\text{CO}_2$  (Andrews 1869)

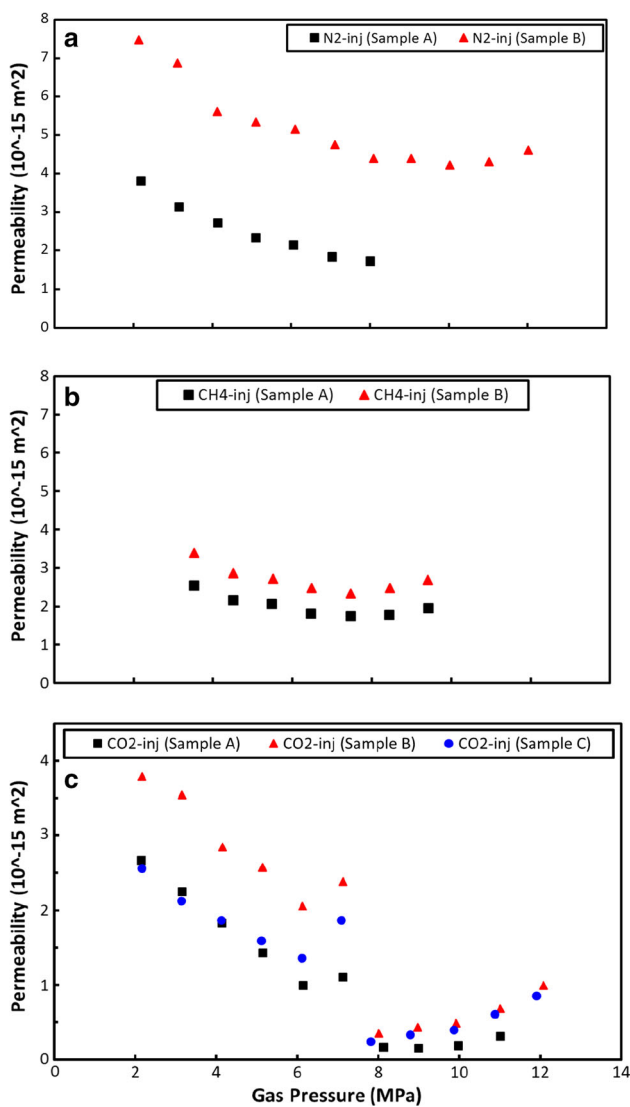


Fig. 12 Permeability evolution in different GRS specimens on injection of  $\text{N}_2$ ,  $\text{CH}_4$ ,  $\text{CO}_2$ . The observations were made on incrementing gas pressures at constant confining pressure of 20 MPa

Three different specimens are measured, namely monolayered, multilayered (four layers of proppant) and pre-experiment specimens (used as control). Only one embedment surface of the two halves of each specimen is profiled since the surface configuration of the two halves is complementary to each other. Three random observation windows with a  $1.6 \text{ mm} \times 1.6 \text{ mm}$  window are captured from the surface of each specimen for measurement (Fig. 14). Results are analyzed statistically with error bars (Fig. 16).

**3.2.6.1 Roughness** Surface roughness refers to the third up to the sixth order deviation from the nominal surface with all different order deviations superimposed to form the surface roughness profile. The embedment of proppant into the surface of the fracture is manifest as a measurable surface roughness that may be characterized by a variety of surface roughness parameters (Fig. 15). These include the arithmetic average (the roughness profile contains  $n$  orders) of the absolute values of the profile height  $y_i$  deviations from the mean line, recorded within the evaluation length  $l$  ( $S_a$ ; Eq. 10) as the most common. Other common parameters include root-mean-square (RMS)  $S_q$  (Eq. 11) and the average distance between the highest peak  $S_p$  and lowest valley  $S_v$  in each sampling length  $S_z$  (Eq. 13). RMS, which also known as  $S_q$ , is the root-mean-square average of the profile height  $y_i$  deviations from the mean line, recorded within the evaluation length  $l$  (Eq. 11).

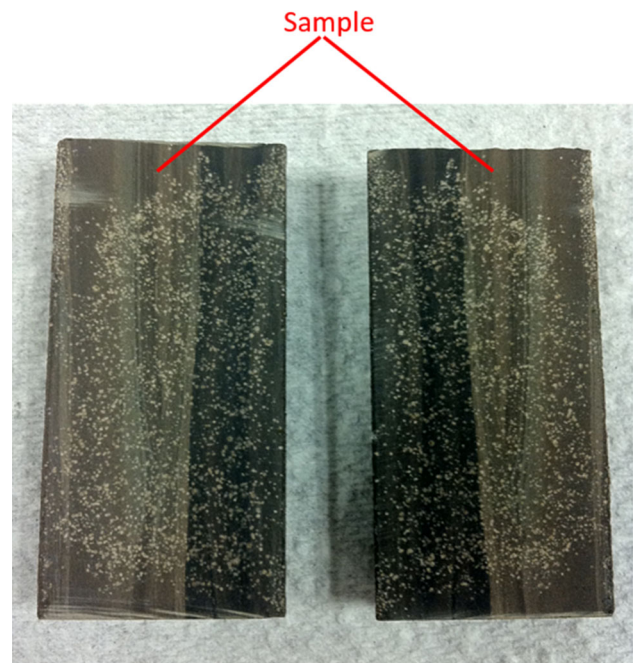
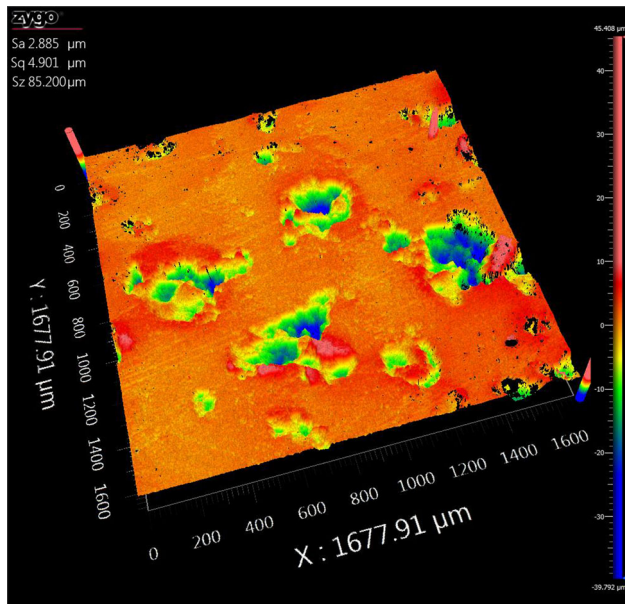


Fig. 13 Proppant embedment (shown as white indentations) after a test (monolayer specimen)



**Fig. 14** View of embedment surface on specimen propped with four layers of proppant

Here, surface roughness is characterized by  $S_a$ ,  $S_q$  and  $S_z$ .

$$S_a = \frac{1}{n} \sum_{i=1}^n |y_i| \tag{10}$$

$$S_q = \sqrt{\frac{1}{n} \sum_{i=1}^n y_i^2} \tag{11}$$

$$S_t = S_p - S_v \tag{12}$$

$$S_z = \frac{1}{l} \sum_{i=1}^s S_{t_i} \tag{13}$$

where the roughness profile (Fig. 15) contains  $n$  orders, equally spaced points at the cutoff of the 1st sampling length to the  $i$ th sampling length along the trace;  $y_i$  is the vertical distance from the mean line to the  $i$ th data point;  $S_p$  is the maximum peak height;  $S_v$  is the maximum valley depth;  $l$  is the sampling lengths; and  $S_{t_i}$  is  $S_t$  for the  $i$ th sampling length.

A simplified investigation is conducted where three profiles on each sample are taken for measurement, and then the averages of  $S_a$ ,  $S_q$  and  $S_z$  are calculated, respectively. The average  $S_a$ ,  $S_q$  and  $S_z$  values for specimens propped with four layers, for a single layer of proppant and for pre-experiment specimen are summarized in Table 1 below.

In Fig. 16, the error bars indicate the uncertainty of the measurement. The error bars shown in the line graph above simply represent the range of experimental data. Figure 16a–c shows that there is a significant difference between these three specimens. The pre-experiment specimen is the smoothest, with no embedment. Swelling effects are reversible, whereas embedment due to plasticizing of the organic component, or due to destructive indentation, is likely irreversible (Meyers 1982). Therefore, we conclude that the monolayer propped specimen has the highest roughness due to the most significant embedment effect compared to the multilayered specimen (Fig. 17).

### 4 Conclusions

Experiments have been conducted on Green River Shale with both mono- and multilayered proppants, and concurrently with measurements of permeability evolution as a

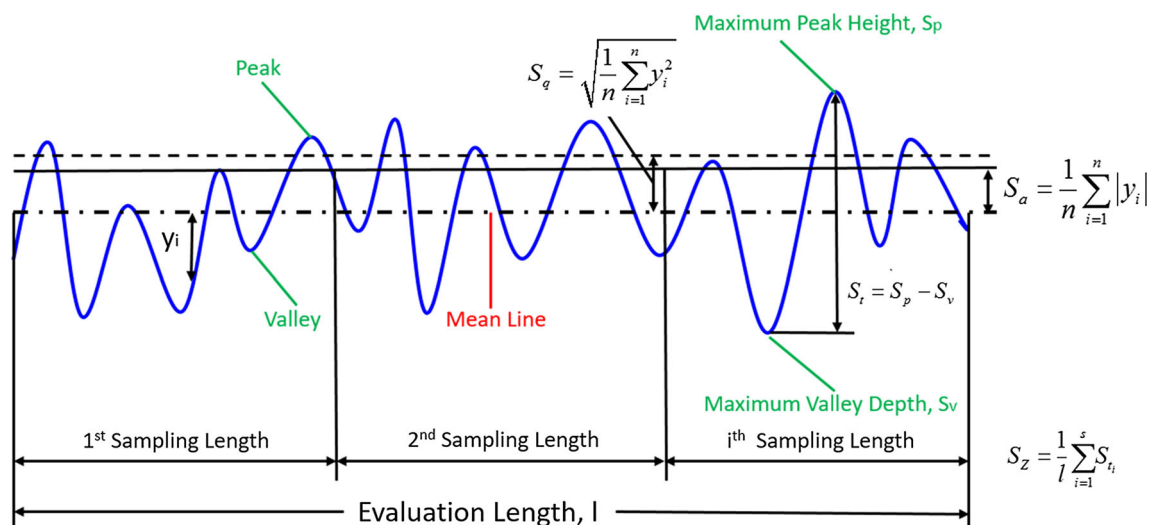


**Fig. 15** Surface roughness profile

**Table 1** Average  $S_a$ ,  $S_q$  and  $S_z$  values for specimens propped with four layers, for a single layer of proppant and for pre-experiment specimen

	Four layered proppant	Single layered proppant	Pre-experiment
$S_a$ ( $\mu\text{m}$ )	2.85	4.65	0.41
$S_q$ (RMS) ( $\mu\text{m}$ )	4.81	8.42	0.55
$S_z$ ( $\mu\text{m}$ )	69.49	99.11	16.28

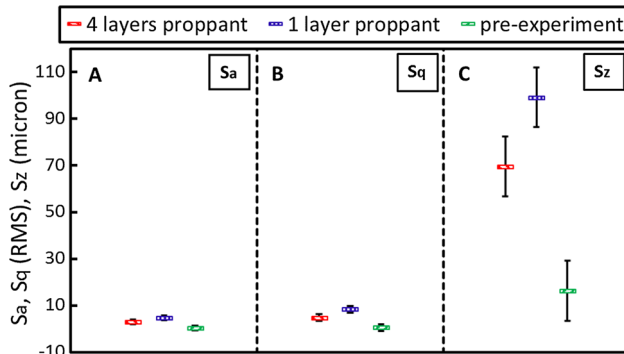


**Fig. 16**  $S_a$ ,  $S_q$  (RMS) and  $S_z$  of embedment surface of multilayered (red), monolayered (blue) specimens and pre-experiment specimens (green) as a control (color figure online)

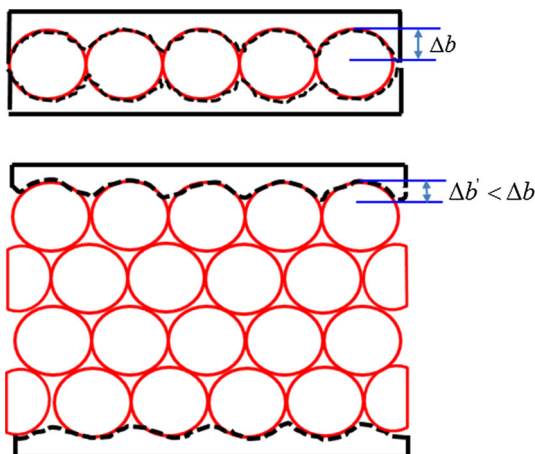


**Fig. 17** Comparison on the change of aperture between monolayered and multilayered specimen

function of fluid pressure for  $\text{CO}_2$ ,  $\text{CH}_4$ ,  $\text{N}_2$  and He. The findings are as follows:

1. The permeability of propped fractures first decreases with increasing gas pressure (decreasing effective stress) for adsorptive gases including  $\text{CO}_2$ ,  $\text{CH}_4$  and  $\text{N}_2$ , indicating the potentially dominant role of swelling due to adsorption and the greater effect of swelling compared to that of mechanical dilation. When this decrease reaches a threshold pressure (expected to be approximately twice the Langmuir pressure), permeability rebounds and then increases with increasing gas pressure, suggesting that mechanical dilation due to decreased effective stress dominates over swelling

effects. The competition between swelling and mechanical dilation results in a typical U-shaped curve of permeability versus pressure for adsorptive gases. Results also indicate that the Langmuir pressure of  $\text{CO}_2$  is lower than that of  $\text{CH}_4$  in Green River Shale. For cases using non-adsorptive He as a permeant, permeability monotonically increases with gas pressure with no adsorption-induced swelling observed. Permeability magnitudes are similar for all four gasses at  $\sim 10^{-15} \text{ m}^2$ .

2. Permeability to  $\text{CO}_2$  drops by 63% of the initial permeability when effective stress decreases by 6 MPa. Permeability to  $\text{CH}_4$  decreases by 31% and to  $\text{N}_2$  decreases by 54% when effective stress decreases by 8 MPa.
3. Compared to the multilayered propped specimen, the monolayered propped specimen exhibits a larger swelling effect and has a greater roughness.
4. The duration of gas exposure and saturation, over the timescale of our experiments (about 20 h), does not exert a significant influence on permeability for adsorptive or non-adsorptive gases. However, this may be an effect of the limited time (duration) of exposure; we expect time-dependent swelling effects if gas is able to diffuse into the rock matrix after considerably longer time.
5. Permeability measured for both injection and depletion cycles generally overlap and are repeatable, with little hysteresis. Permeability of different specimens has the same magnitude and trend.

**Acknowledgements** This work was supported by Aramco Services Company. This support is gratefully acknowledged. We also thank Takuya Ishibashi for his assistance with fracture surface roughness measurement.

## References

- Alramahi B, Sundberg MI (2012) Proppant embedment and conductivity of hydraulic fractures in shales. American Rock Mechanics Association, Chicago
- Andrews T (1869) On the continuity of the gaseous and liquid states of matter. Philos Trans 159:575–590
- Bai M, Elsworth D (1994) Modeling of subsidence and stress-dependent hydraulic conductivity for intact and fractured porous media. Rock Mech Rock Eng 27:209–234
- Berryman JG (1981) Elastic wave propagation in fluid-saturated porous media. J Acoust Soc Am 69:416–424

- Brace WF, Walsh JB, Frangos WT (1968) Permeability of granite under high pressure. *J Geophys Res* 73(6):2225–2236
- Carman PC (1937) Fluid flow through granular beds. *Trans Inst Chem Eng Lond* 15:150–166
- Chandra C (2012) Mechanical and transport characteristics of coal-biomass mixtures for advanced IGCC systems. PennState MS Thesis
- Chen T, Feng X, Pan Z (2015) Experimental study of swelling of organic rich shale in methane. *Int J Coal Geol* 150–151(1):64–73
- Cooke CE (1977) Hydraulic fracturing with a high-strength proppant. *J Petrol Technol* 29:1222–1226
- Elsworth D, Yasuhara H (2010) Mechanical and transport constitutive models for fractures subject to dissolution and precipitation. *Int J Numer Anal Methods Geomech* 34:533–549
- Freeman ER, Anschutz DA, Rickards AR, Callanan MJ (2009) Modified API/ISO crush tests with a liquid-saturated proppant under pressure incorporating temperature, time, and cyclic loading: What does it tell us?. *SPE Hydraulic Fracturing Technology Conference Society of Petroleum Engineers, The Woodlands*
- Haro C (2013) The theory behind the Carman–Kozeny equation in the quest for permeability of the Rocks. In: *GeoConvention: Integration, 5th–10th May, Calgary, Canada*
- Heller R, Zoback M (2014) Adsorption of methane and carbon dioxide on gas shale and pure mineral samples. *J Unconv Oil Gas Resour* 8:14–24
- Hsieh PA et al (1981) A transient laboratory method for determining the hydraulic properties of ‘tight’ rocks—I. Theory. *Int J Rock Mech Min Sci Geomech Abstr* 18(3):245–252
- Kozeny J (1927) Ueber kapillare Leitung des Wassers im Boden. *Sitzungsber Akad Wiss* 136(2a):271–306
- Kumar H, Elsworth D, Mathews JP, Marone C (2016) Permeability evolution in sorbing media: analogies between organic-rich shale and coal. *Geofluids* 16(1):43–55
- Lacy LL, Rickards AR, Ali SA (1997) Embedment and fracture conductivity in soft formations associated with HEC, borate and water-based fracture designs. *SPE Annual Technical Conference and Exhibition, San Antonio*
- Meyers RA (1982) The macromolecular structure of coal: coal structure. Academic Press Inc., New York, p 250
- Pellenq RJ, Brochard L, Damme MV, Ulm FJ (2012) From the fundamentals of porous carbons poromechanics to applications for CO<sub>2</sub> sequestration and gas-shale. Pittsburgh, AIChE
- Piggott AR, Elsworth D (1993) Laboratory assessment of the equivalent apertures of a rock fracture. *Geophys Res Lett* 20:1387–1390
- Rose HE (1945) An investigation into the laws of flow of fluids through granular material. *Proc Inst Mech Eng* 153:141–148
- Shimada S, Li H, Oshima Y, Adachi K (2005) Displacement behavior of CH<sub>4</sub> adsorbed on coals by injecting pure CO<sub>2</sub>, N<sub>2</sub>, and CO<sub>2</sub>–N<sub>2</sub> mixture. *Environ Geol* 49:44–52
- Siriwardane H et al (2009) Influence of carbon dioxide on coal permeability determined by pressure transient methods. *Int J Coal Geol* 77:109–118
- Slichter CS (1899) Theoretical investigation of the motion of ground water. *US Geol. Survey 19th Ann. Rept., Vol pt. 2*, pp 295–384
- Somerton WH, Soylemezoglu IM, Dudley RC (1975) Effect of stress on permeability of coal. *Int J Rock Mech Min Sci Geomech Abstr* 12:129–145
- Stoddard T, McLennan T, Moore J (2011) Fracture conductivity of a bauxite-propped geothermal system at in situ conditions. In: *Thirty-Sixth Workshop on Geothermal Reservoir Engineering, Stanford University, Stanford*
- Walsh JB (1981) Effect of pore pressure and confining pressure on fracture permeability. *Int J Rock Mech Min Sci Geomech Abstr* 18:429–435
- Wang S, Elsworth D, Liu J (2011) Permeability evolution in fractured coal: the roles of fracture geometry and water-content. *Int J Coal Geol* 87:13–25
- Yasuhara H, Elsworth D (2008) Compaction of a rock fracture moderated by competing roles of stress corrosion and pressure solution. *Appl Geophys* 165:1289–1306
- Yasuhara H et al (2006) Evolution of fracture permeability through fluid–rock reaction under hydrothermal conditions. *Earth Planet Sci Lett* 244:186–200